MDPI

Article

Comparison of Magnesium and Titanium Doping on Material Properties and pH Sensing Performance on Sb_2O_3 Membranes in Electrolyte-Insulator-Semiconductor Structure

Chyuan-Haur Kao [1,2,3], Kuan-Lin Chen [1], Jun-Ru Chen [4], Shih-Ming Chen [4], Yaw-Wen Kuo [5], Ming-Ling Lee [6,*], Lukas Jyuhn-Hsiarn Lee [7] and Hsiang Chen [4,*]

[1] Department of Electronic Engineering, Chang Gung University, 259 Wen-Hwa 1st Road, Kwei-Shan District, Tao Yuan City 333, Taiwan; chkao@mail.cgu.edu.tw (C.-H.K.); klchen@mail.ncku.edu.tw (K.-L.C.)
[2] Kidney Research Center, Department of Nephrology, Chang Gung Memorial Hospital, Chang Gung University, No. 5 Fuxing St., Guishan District, Taoyuan City 333, Taiwan
[3] Department of Electronic Engineering, Ming Chi University of Technology, 284 Gungjuan Rd., Taishan Dist., New Taipei City 243, Taiwan
[4] Department of Applied Materials and Optoelectronic Engineering, National Chi Nan University, Puli 545, Taiwan; s107328002@mail1.ncnu.edu.tw (J.-R.C.); s107328009@mail1.ncnu.edu.tw (S.-M.C.)
[5] Department of Electrical Engineering, National Chi Nan University, Puli 545, Taiwan; ywkuo@ncnu.edu.tw
[6] Department of Electro-Optical Enginnering, Minghsin University of Science and Technology, No.1, Xinxing Rd., Xinfeng 304, Taiwan
[7] National Institute of Environmental Health Sciences, National Health Research Institutes, Zhunan 350, Taiwan; lukaslee@nhri.edu.tw
* Correspondence: mingling@must.edu.tw (M.-L.L.); hchen@ncnu.edu.tw (H.C.)

Abstract: In this research, electrolyte-insulator-semiconductor (EIS) capacitors with Sb_2O_3 sensing membranes were fabricated. The results indicate that Mg doping and Ti-doped Sb_2O_3 membranes with appropriate annealing had improved material quality and sensing performance. Multiple material characterizations and sensing measurements of Mg-doped and Ti doping on Sb_2O_3 sensing membranes were conducted, including of X-ray diffraction (XRD), X-ray photoelectron spectroscopy (XPS) and transmission electron microscopy (TEM). These detailed studies indicate that silicate and defects in the membrane could be suppressed by doping and annealing. Moreover, compactness enhancement, crystallization and grainization, which reinforced the surface sites on the membrane and boosted the sensing factor, could be achieved by doping and annealing. Among all of the samples, Mg doped membrane with annealing at 400 °C had the most preferable material properties and sensing behaviors. Mg-doped Sb_2O_3-based with appropriate annealing are promising for future industrial ionsensing devices and for possible integration with Sb_2O_3-based semiconductor devices.

Keywords: Mg doping; Ti doping; pH sensing; Sb_2O_3; silicate; crystallization

1. Introduction

Over the past fifty years, growing attention has been paid to the development of the chemical sensing of ion concentrations in various solutions. Measurements of ion concentrations, such as pH sensing, are crucial to monitor human health, food safety and environmental pollution. Owing to rapid detection, fast response and reliable long-term operations, semiconductor-based ion sensitive devices have been proposed, such as ion-sensitive field-effect transistors (ISFETs), electrolyte-insulator -semiconductor (EIS) capacitors and light-addressable potentiometric sensors (LAPS-) [1,2]. Among these devices, EIS capacitors, with their advantages of compact size, low cost and simple fabrication, have been demonstrated as multianalyte ion and solute sensing devices [3,4]. In an EIS capacitor, the key component is the sensing membrane, capable of detecting ions in solutions. For conventional EIS devices, SiO_2 is commonly used as the dielectric for the membrane, though materials such as Ta_2O_5 [5], Gd_2O_3 [6] and Zr_2O_3 have also been studied as possible

replacements for traditional SiO_2. In order to further boost the EIS capacitor's performance and provide the possibility for future device integration, it is worthwhile to explore new materials and treatments for the membrane material in order to fabricate EIS capacitors with pH-sensing behaviors. Based on previous reports [7,8], Sb_2O_3 has been used for transparent conducting films, varistors and photocatalysts. In addition, the usage of Sb_2O_3 can improve electrical and optical device properties. Based on recent studies [9–19] Sb_2O_3 has been used for gas and liquid solution sensors. However, Sb_2O_3 EIS sensors have not been clearly reported yet. Compared with conventional semiconductor materials, Sb_2O_3 with a wide band gap of around 3 eV [20] can withstand high breakdown voltage. As for new treatments, incorporating various atoms such as F [21], N [22], Ti [23] and Mg [24] by plasma treatment [25] or co-sputtering [26] into EIS membranes to strengthen their material quality has been intensively investigated. For foreign atoms dopings, Ti doping and Mg doping via cosputtering can optimize the EIS sensor's sensing behaviors because the incorporated atoms can passivate defects. Moreover, Mg doping could further boost the sensitivity and reliability of EIS sensors, owing to the decrease of the double-layer capacitance in the solution and sensing factor enhancement. Until now, however, comparison of the effects of Mg doping and Ti doping on EIS membranes has not been demonstrated. In this study, Mg-doped and Ti-doped Sb_2O_3 were fabricated as membranes with excellent sensing performance. However, EIS capacitors with Mg-doped or Ti-doped Sb_2O_3 [27–35] as the membrane material have not been clearly reported yet. Since Mg has low electron affinity and low electronegativity, and the radius of Mg^{2+} is similar to that of Sb^{3+}, Mg can perfectly replace the lattice site of Sb [36–43]. In addition, many studies have also shown that Mg doping can increase the energy gap and reduce redundant oxygen vacancies. Moreover, annealing treatment in an O_2 ambient can further improve sensing performance and device reliability. This is because filling the oxygen vacancy and reducing the defects in an oxygen environment repairs the dangling bonds and releases the strain bonds, while more oxygen atoms are added to the surface and the oxygen vacancies in the lattice are filled. Therefore, Mg-doped Sb_2O_3 EIS sensors with annealing at 400 °C can achieve a high sensitivity of 60.17 mV/pH, which is above the Nernst limit [44]. To gain insight into the effects of annealing, multiple material analyses including X-ray diffraction (XRD), X-ray photoelectron sptroscopy (XPS) and field-effect scanning electron microscopy (FESEM) were used to examine the surface morphologies and material properties of Sb_2O_3 membranes. Material characterizations reveal that annealing at an appropriate temperature can enhance Sb_2O_3 crystallization and Ti doping of the Sb_2O_3, and Mg doped of the Sb_2O_3 can suppress the formation of silicate grainization. Therefore, the EIS pH-sensing capability could be boosted and reliability issues such as hysteresis and drift voltage can be mitigated. Mg-doped Sb_2O_3-based EIS capacitors are promising for versatile integration in chemical ion-sensing applications with other Sb_2O_3-based devices [45–48].

2. Experimental

To fabricate Sb_2O_3-based EIS capacitors, the films were deposited on 4-inch n-type (100) wafers with a resistivity of 5–10 Ω-cm. The Sb_2O_3 was sputtered, and Mg or Ti was co-sputtered on the wafers in an Ar:O_2 = 20:5 ambient, respectively. The RF power was l00 W and the pressure inside the chamber was l0 mTorr. Based on the measurements, the thickness of the undoped Sb_2O_3 was 61.53 nm, the thickness of Mg-doped Sb_2O_3 was 63.40 nm and the thickness of the Ti-doped Sb_2O_3 was 69.25 nm. The rapid thermal annealing (RTA) process was carried out for 30 s in O_2 ambient at temperatures of 400, 500 and 600 °C, respectively. Then, a 300 nm aluminum film was deposited on the backside of the wafer. The backside aluminum film was grown by e-beam evaporation. After that, an epoxy bond was used to determine the sensing area. Finally, silver gel was used to attach samples on the copper wires of the printed circuit board (PCB). The detailed EIS structure is shown in Figure 1.
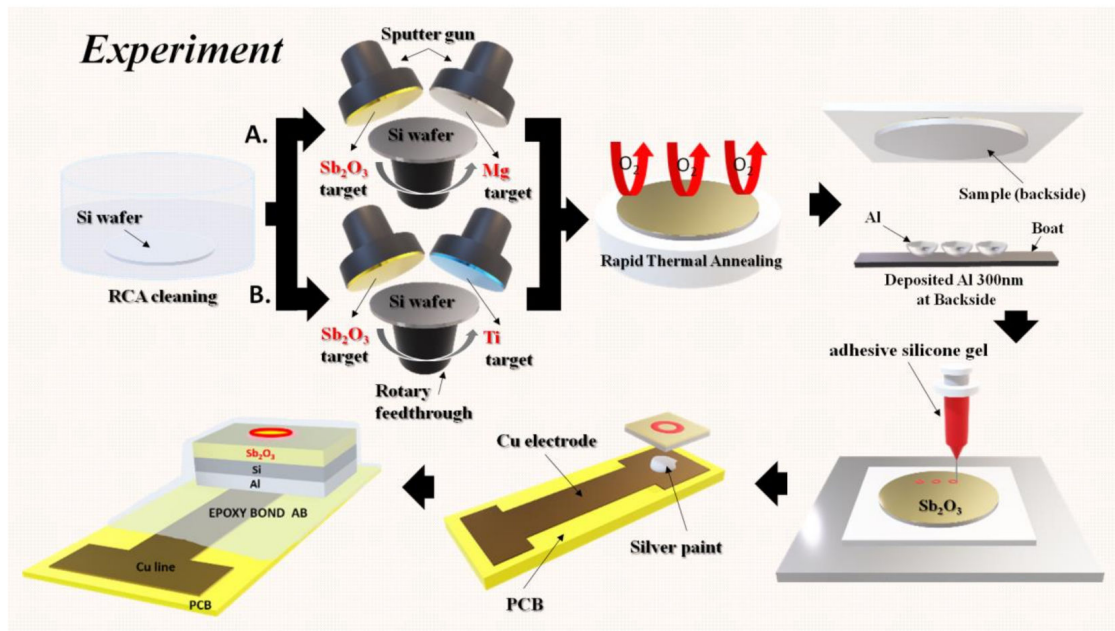
Figure 1. A diagram of the fabrication process including, RCA cleaning, co-sputtering, rapid thermal annealing, aluminum film backside deposition, sensing area definition and the attachment of the sensing chip onto the PCB board.

Analyses using CV measurements were performed. Using a reference capacitance of 0.4 C_{max} in the CV curves, the correlation between the substrate bias and the electrolyte concentration was calculated. In addition, the change of substrate bias voltage variation caused by the change of electrolyte concentration can be illustrated by the site-binding model [49,50], with the flat band voltage shift proportional to the electrolyte concentration, as in the following equation:

$$V_{FB} = E_{Ref} - \Psi_0 + \chi^{sol} - \frac{\Phi_{Si}}{q} - \frac{Q_{ox} - Q_{ss}}{C_{ox}} \qquad (1)$$

E_{Ref} is the reference electrode potential, and χ^{sol} is the surface dipole potential of the solution. Φ_{Si} is the work function of silicon, and Ψ_0 is the liquid junction potential difference. All of the terms in the equation are constant, except for Ψ_0, which makes the membrane sensitive to the electrolyte due to polarization and forms the potential barrier. Furthermore, Ψ_0 is closely related to the surface sites on the membrane.

Moreover, the hydrogen ionic reaction with the membrane interface is illustrated in the site-binding model shown in Equation (2) [51–53]. The surface potential (ψ) can be related to the membrane parameter β. k is Boltzmann's constant, q is the elementary charge, T is the temperature, pH_{pzc} is the pH value with zero charge on the surface and β is a factor that points to the sensitivity of the gate membrane.

$$\psi = 2.303 \frac{kT}{q} \frac{\beta}{\beta + 1} (pH_{pzc} - pH) \qquad (2)$$

Furthermore, β is closely related to the density of surface hydroxyl groups, as shown in (3). N_s is the number of surface sites per unit surface area and C_{DL} is the double layer capacitance, according to the Gouy–Chapman–Stern model [54].

$$\beta = \frac{2q^2 Ns \sqrt{K_a K_b}}{KT C_{DL}} \qquad (3)$$

In this research, Mg-doped Sb_2O_3-based EIS capacitors were demonstrated as the best pH-sensing devices, as shown in Figure 2. The tighter inner layer becomes the Helmholtz layer, which causes the positive charge to be absorbed by the Helmholtz layer and is not affected by the potential difference.
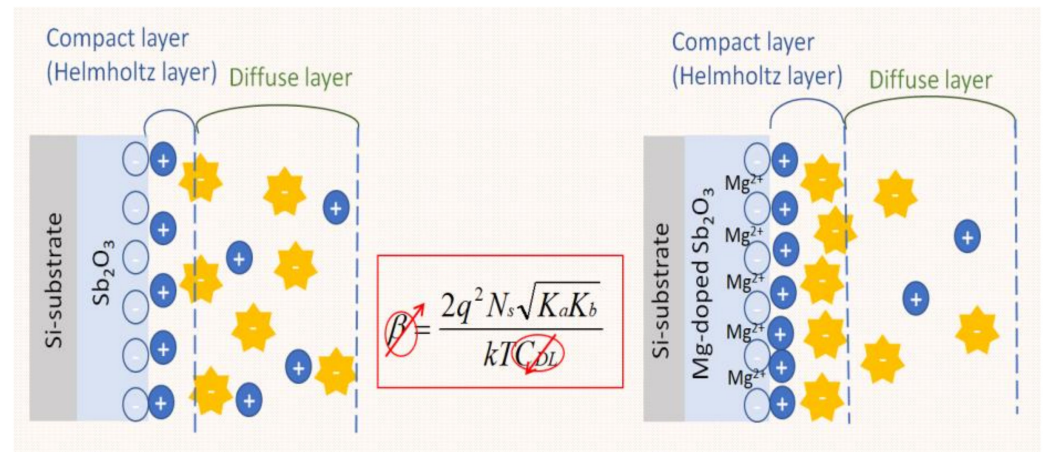

Figure 2. An illustration of the Mg co-sputtered on the Sb_2O_3-based EIS capacitor.

Therefore, the outer layer is still a diffusion layer, and the resulting capacitance C_{DL} is reduced. It is known from the Moss-Berstein effect that, when the capacitance C_{DL} decreases, the β value increases, so, the higher β is, the better the sensing capability will be [55,56].

Based on (3), the higher the surface site density of N_s is, the higher β is and the better the sensing capability will be. The grainization, crystallization and compactness of the material structure on the sensing membrane may reinforce the quality and quantity of the surface sites.

3. Results and Discussion

To investigate the effects of Ti doping and Mg doping with annealing on a Sb_2O_3 membrane, XRD was used to monitor the crystalline phases of the differently treated films. The XRD patterns of the undoped, Ti-doped and Mg-doped samples are shown in Figure 3a–c, respectively. As shown in Figure 3a–c, Sb_2O_3 (222), (400) and (440) phases can be observed in the XRD patterns of all of the samples. Among the undoped samples, the film annealed at 500 °C had the strongest crystalline phases. In addition, among Ti-doped and Mg-doped samples, the samples annealed at 400 °C had the strongest crystallized phases. Furthermore, Ti-doped and Mg-doped samples had stronger XRD peaks than the undoped samples, indicating that the combination of doping could further enhance the crystallization. However, as the anneal temperature increased to 400 and 500 °C, all of the Sb_2O_3 peaks increased, indicative of the crystalline phases strengthening and the crystallization enhancing. As the annealing temperature increased to 600 °C, the Sb_2O_3 decreased, and the crystalline structures might be deteriorated in undoped, Ti-doped and Mg-doped samples owing to the RTA pH-sensing devices at 600 °C.

Furthermore, to monitor the chemical bindings and element compositions, the O 1s XPS analysis was performed on the undoped, Ti-doped and Mg-doped samples, as shown in Figure 4a–c, respectively. Figure 4a reveals that an RTA at an appropriate temperature of 500 °C could effectively suppress the formation of silicate and optimize the sensing device's performance. However, as the annealing temperature further increased to 600 °C, the amount of silicate increased again. Similarly, annealing at 400 °C could effectively suppress the formation of silicate, as shown in the XPS spectra of Ti-doped and Mg-doped samples, as shown in Figure 4b,c. Moreover, annealing could strengthen Sb-O-Ti bonds and Sb-O-Mg bonds in Ti-doped and Mg-doped samples, respectively. Furthermore, the

Sb 3d XPS analysis was performed on the undoped, Ti doped and Mg doped samples, as shown in Figure 4d–f, respectively. The Sb-O doublet peaks can be observed on these spectra. The Sb 3d XPS spectra also show that the Sb-O bonds could be strengthened with an appropriate annealing temperature of 500 °C for the undoped sample, as shown in Figure 4d. In addition, Mg doping could further enhance the Sb-O bonds in terms of Sb-O doublet peaks compared with the undoped samples. Consistent with the XRD patterns, silicate could be mitigated and chemical bindings could be enhanced by annealing and Mg doping [57]. Since XPS could complement the XRD analysis and was the technique used to identify the presence of the Mg and Ti bindings, the measurements of the Ti 2p XPS spectra for Ti-doped samples, as shown in Figure 4g, and the Mg 2p spectra for Mg-doped samples, as shown in Figure 4h, were performed, respectively. The results indicate that the XPS peaks for Ti and Mg did not vary a lot in various annealing conditions, but the peaks did represent the presence of Mg and Ti binding.
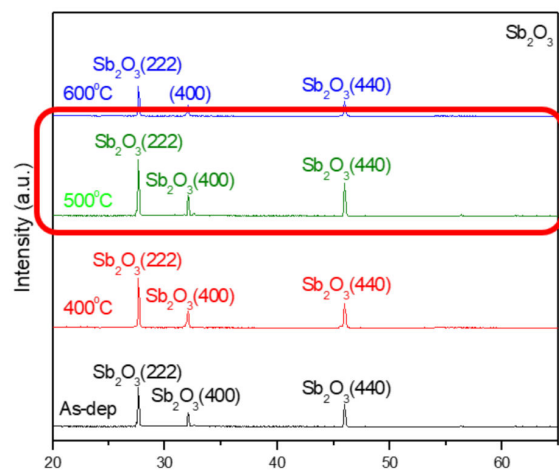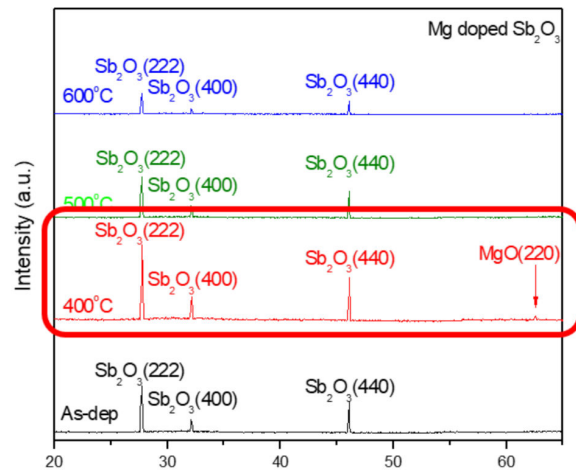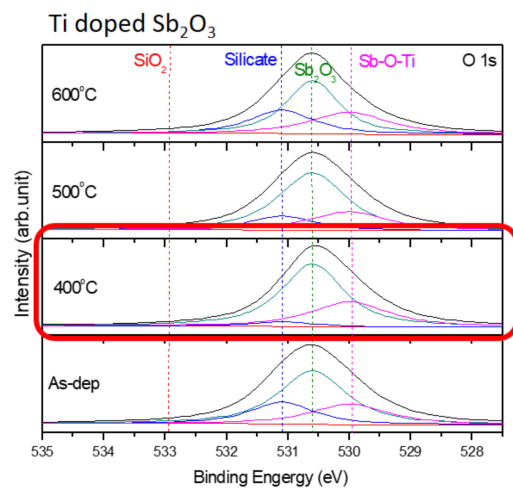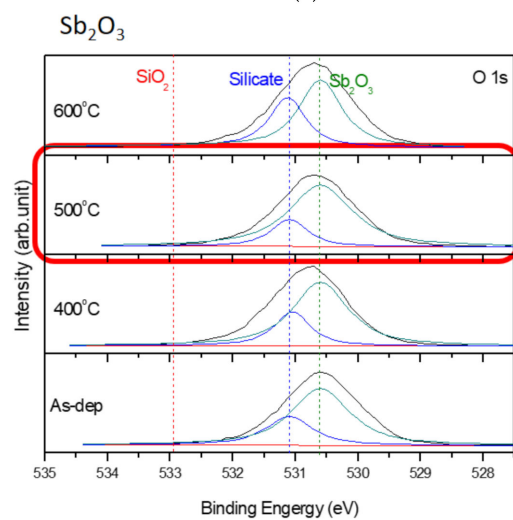

(a)
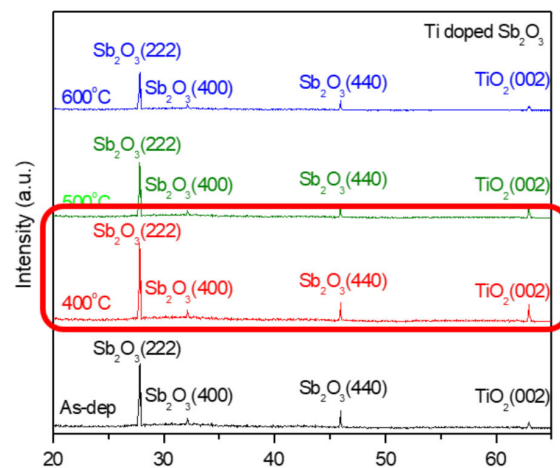
(b)

Figure 3. *Cont.*

(**c**)

Figure 3. XRD patterns of (**a**) the undoped Sb_2O_3 films, (**b**) Ti-doped Sb_2O_3 films and (**c**) Mg-doped Sb_2O_3 films annealed at various temperatures in O_2 ambient for 30 s.
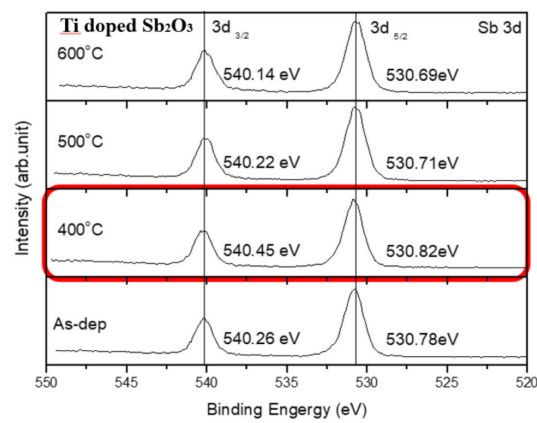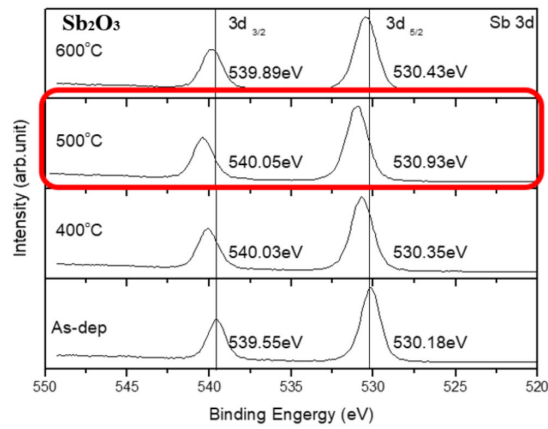

(**a**)

(**b**)

Figure 4. *Cont.*

(**c**)

(**d**)

(**e**)
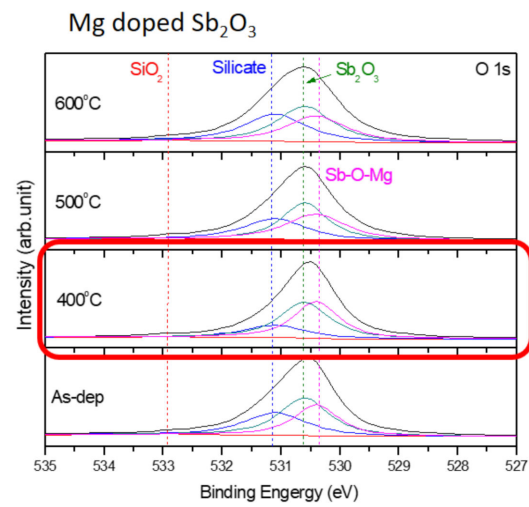
Figure 4. *Cont.*
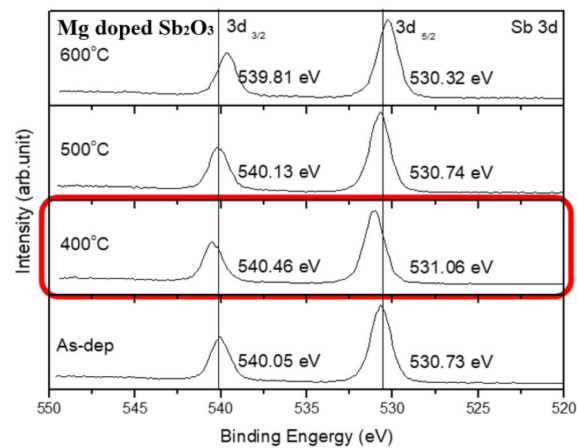
(**f**)
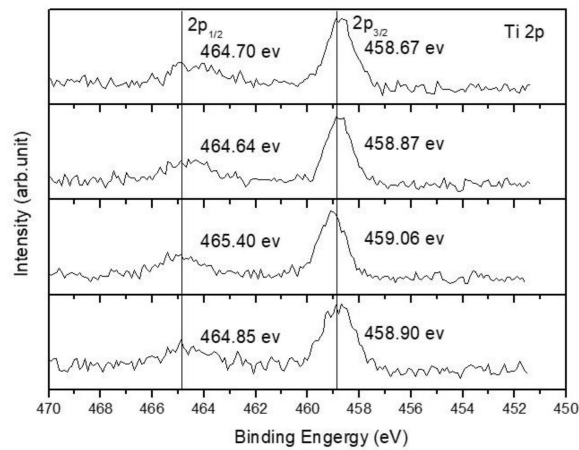
(**g**)
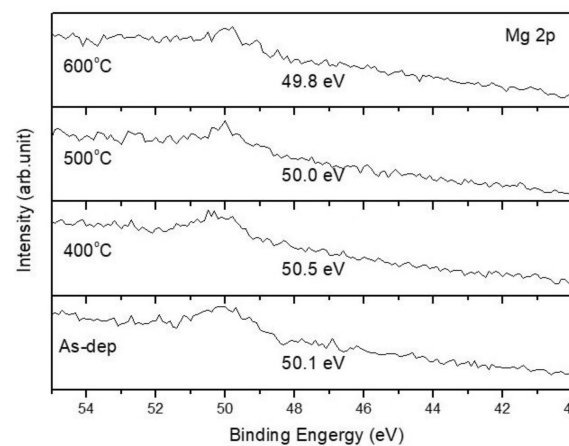
(**h**)

Figure 4. The O 1s XPS spectra of (**a**) the undoped Sb_2O_3 film, (**b**) the Ti-doped Sb_2O_3 films and (**c**) the Mg-doped Sb_2O_3 films. The Sb 3d XPS spectra of (**d**) the undoped Sb_2O_3 film, (**e**) the Ti-doped Sb_2O_3 films and (**f**) the Mg-doped Sb_2O_3 films annealed at various temperatures in O_2 ambient for 30 s. (**g**) The Ti 2p XPS spectra of the Ti doped Sb_2O_3 film. (**h**) The Mg 2p XPS spectra of the Mg doped Sb_2O_3 film.

To examine the nanostructures of the Sb_2O_3 samples, TEM and HRTEM were used to analyze the film in nanometer scale [58]. The TEM and HRTEM images of the as-deposited

Sb_2O_3, the Ti-doped Sb_2O_3 sample annealed at 400 °C, the as-deposited Mg-doped Sb_2O_3 sample and the Mg-doped Sb_2O_3 sample annealed at 400 °C are shown in Figure 5a–d, respectively. The crystalline interval of the as-deposited sample is not clear. As for the annealed Ti-doped sample, the interval spacing can be observed on the TEM image, as shown in Figure 5b. In addition, the enlarged HRTEM image of the interval spacing reveals that the width interval spacing is 0.327 nm, which is close to the 0.322 nm of Sb_2O_3 (222) in a HRTEM image based on a previous report [59]. In addition, the interval spacing of the as-deposited Ti-doped sample can be seen in both the TEM and HRTEM images of Figure 5c. The morphology of the interval spacing of the annealed Ti-doped sample and the as-deposited Mg-doped sample are similar. Compared with the annealed Ti-doped sample and the as-deposited Mg-doped sample, the Mg-doped annealed sample exhibits clearer interval spacing in the TEM and HRTEM images, as shown in Figure 5d. Corresponding with the XRD patterns, as shown in Figure 2, the Mg-doped film annealed at 400 °C had the strongest Sb_2O_3 (222) phases, implying that the combination of Mg doping and annealing could optimize the film's material quality.
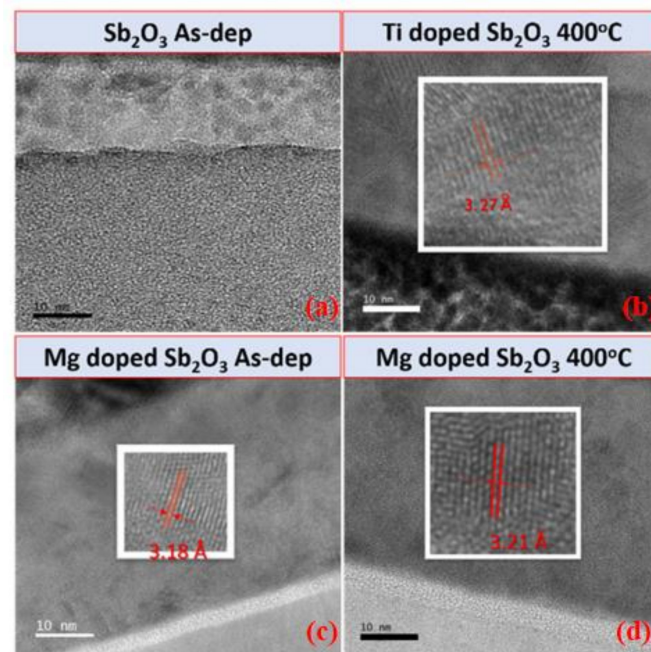

Figure 5. TEM and HRTEM images of (**a**) the as-deposited Sb_2O_3 films, (**b**) the Ti doped Sb_2O_3 film annealed at 400 °C, (**c**) the as-deposited Mg-doped Sb_2O_3 film and (**d**) the Mg-doped Sb_2O_3 film annealed at 400 °C.

To measure the sensitivity and linearity of EIS capacitors, a Ketheley 2400 Source Meter was used to evaluate the C-V curves of the samples treated in various conditions. With 0.4 C_{max} set as the reference capacitance, the sensitivity and linearity could be calculated by extracting the points of various pH values with this reference capacitance. Figure 6a–f show the C-V curves of the EIS capacitors with the as-deposited Sb_2O_3 film and the Sb_2O_3 film annealed at 500 °C, the as-deposited Ti-doped Sb_2O_3 film, the Ti-doped Sb_2O_3 film annealed at 400 °C, the as-deposited Mg-doped film and the Mg-doped Sb_2O_3 film annealed at 400 °C, respectively.
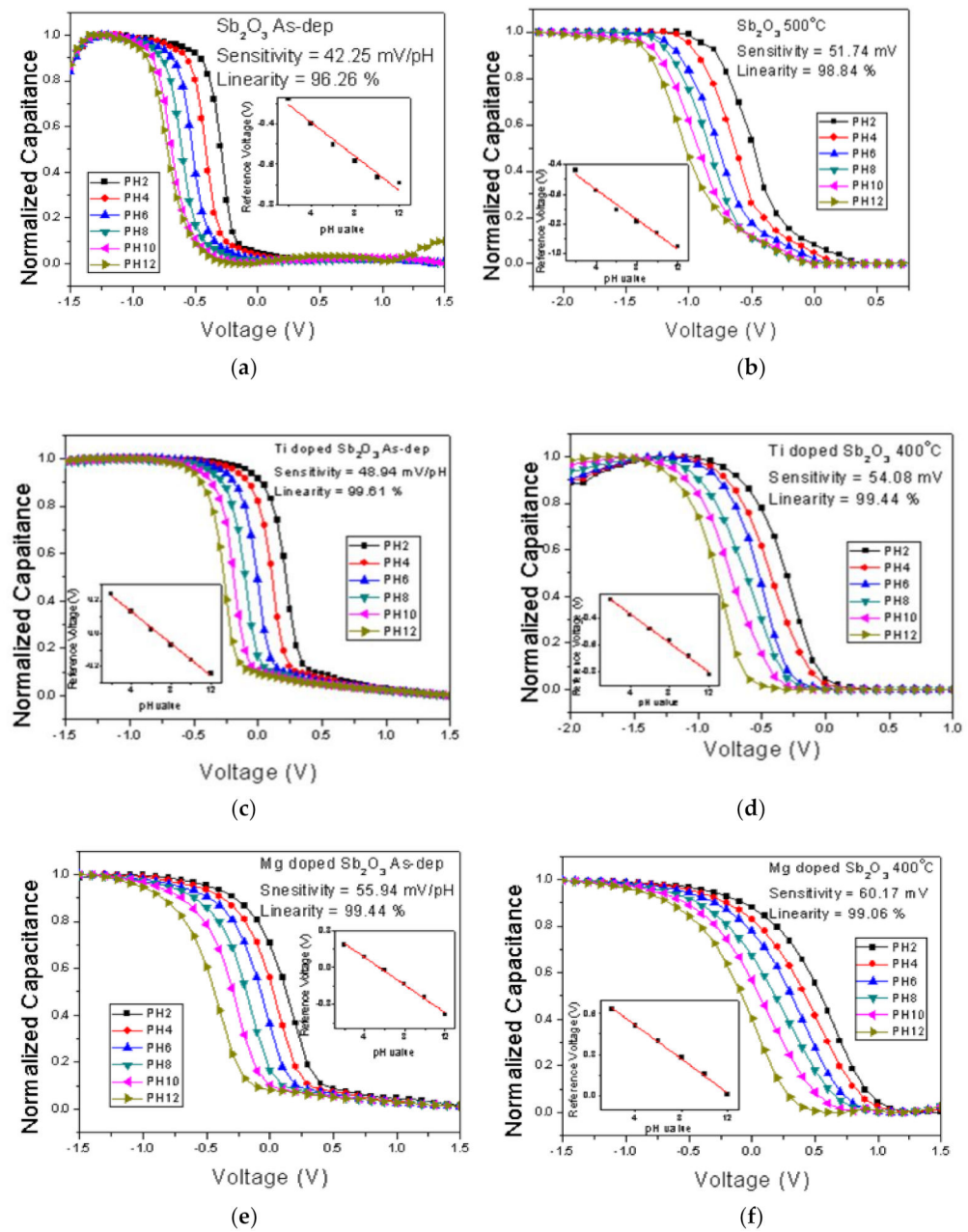
Figure 6. C–V curves of (**a**) the as-deposited Sb_2O_3 sensing membrane, (**b**) the Sb_2O_3 sensing membrane annealed at 500 °C, (**c**) the as-deposited Ti-doped Sb_2O_3 sensing membrane, (**d**) the Ti-doped Sb_2O_3 sensing membrane annealed at 400 °C, (**e**) the as-deposited Mg-doped sensing membrane and (**f**) the Mg-doped O_3 sensing membrane annealed at 400 °C.

Consistent with the material characterizations, the pH sensitivity and linearity of the as-deposited membrane could be improved by annealing at 500 °C, as shown in Figure 6a,b. Moreover, the sensitivity and linearity could also be boosted by Ti doping and Mg doping without annealing, as shown in Figure 6c,e. In addition, appropriate annealing at 500 °C could further enhance the sensitivity of the Ti-doped samples from 48.94 to 54.08 mV/pH and the Mg-doped samples from 55.94 to 60.17 mV/pH, respectively, as shown in Figure 6d,f. All of the linearity and sensitivity data of the undoped, the Ti-doped and the Mg-doped samples treated with various annealing conditions are presented in Figure 7a–c.

(**a**)

(**b**)
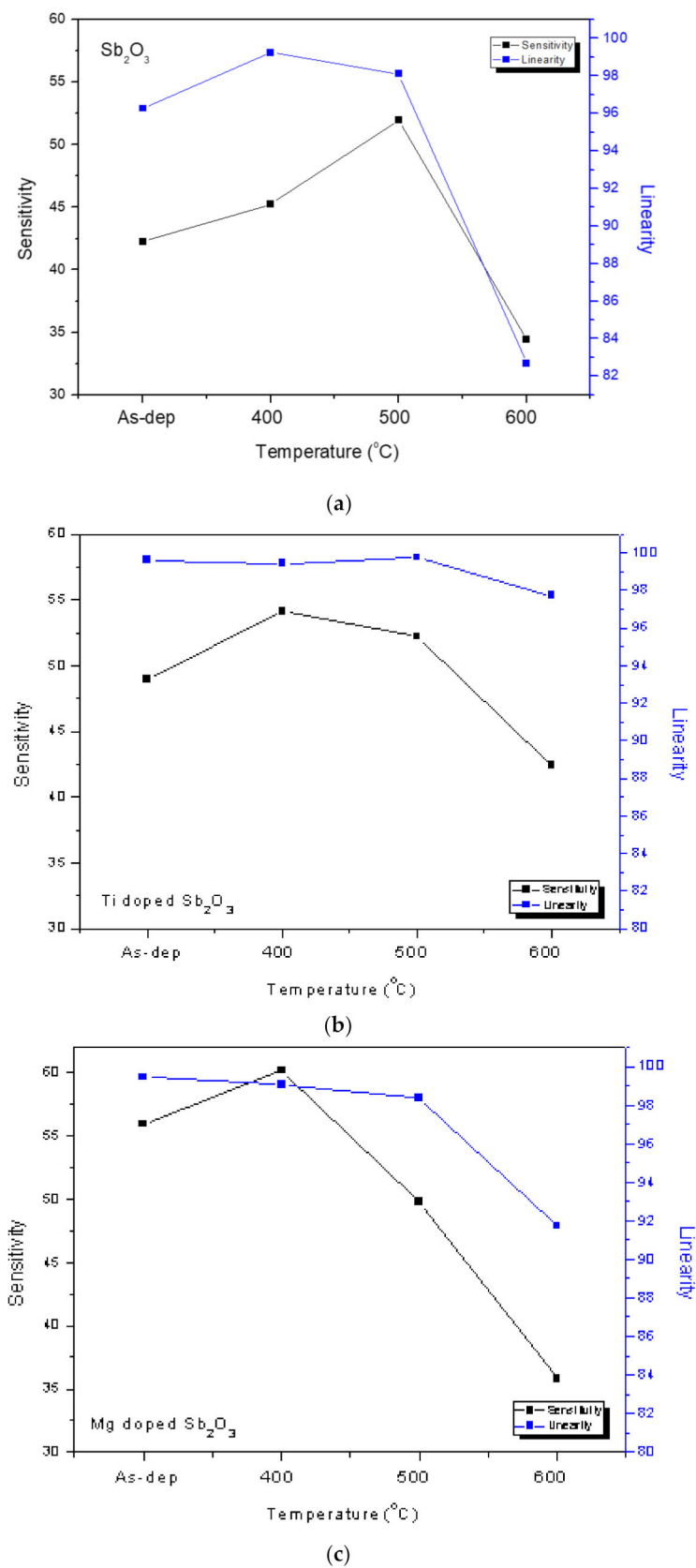

(**c**)

Figure 7. The pH sensitivity and linearity of (**a**) the undoped Sb_2O_3 membrane, (**b**) the Ti-doped Sb_2O_3 membrane and (**c**) the Mg-doped Sb_2O_3 membranes treated with different RTA temperatures in O_2 ambient.

As for the undoped samples, annealing at the appropriate temperatures of 400 °C and 500 °C effectively enhanced the sensitivity and linearity of the membrane, as shown in Figure 8a. Moreover, as shown in Figure 7b,c, in line with all of the material analyses, the combination of doping and appropriate annealing at 400 °C superpositionally increased both sensitivity and linearity for the Ti-doped and Mg-doped samples. Annealing with a high annealing temperature of 600 °C would degrade the material quality and the sensing behaviors of the doped Sb_2O_3 membranes. Material quality improvements enhanced the device sensing properties. Among all of the membranes, the Mg-doped membrane annealed at 400 °C with the strongest crystallization, grainization, and chemical bindings had the best pH sensitivity of 60.17 mV/pH and a high linearity of 99.06% [60,61].
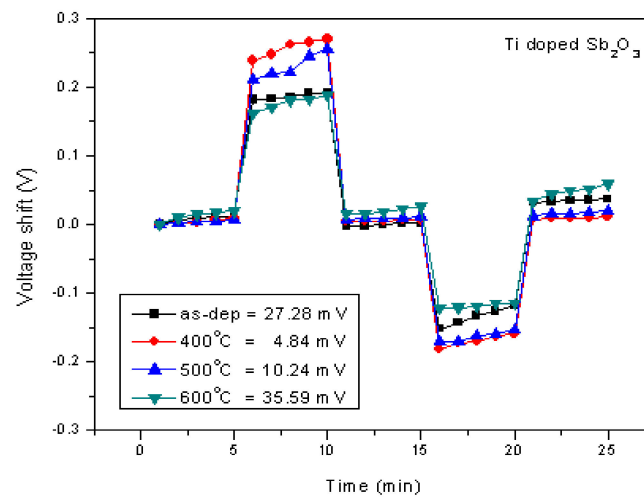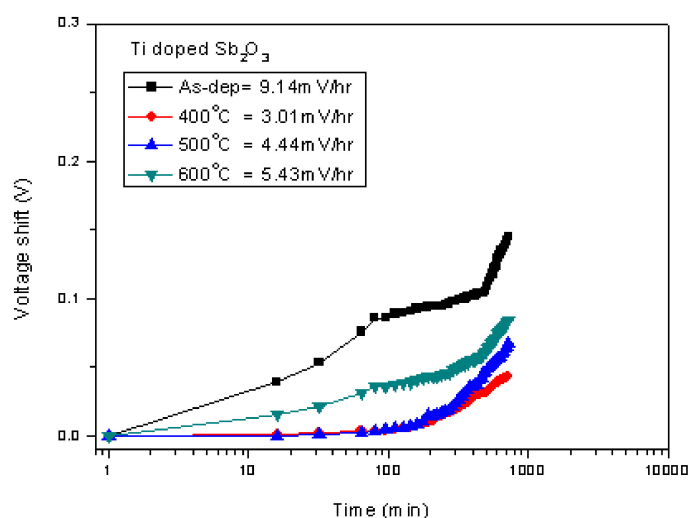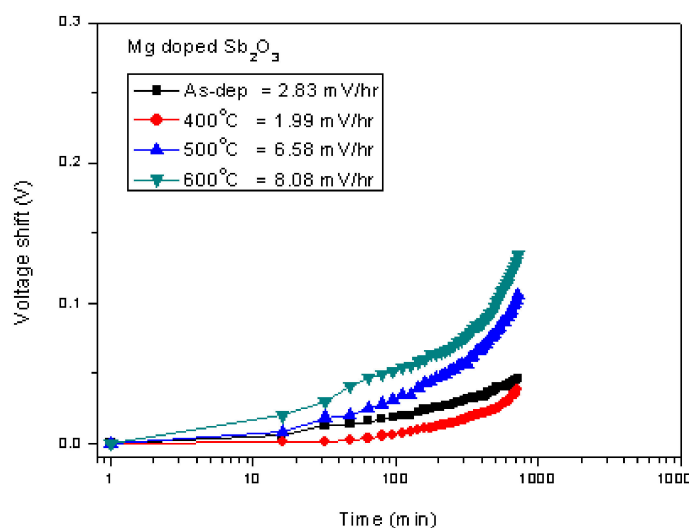

(**a**)
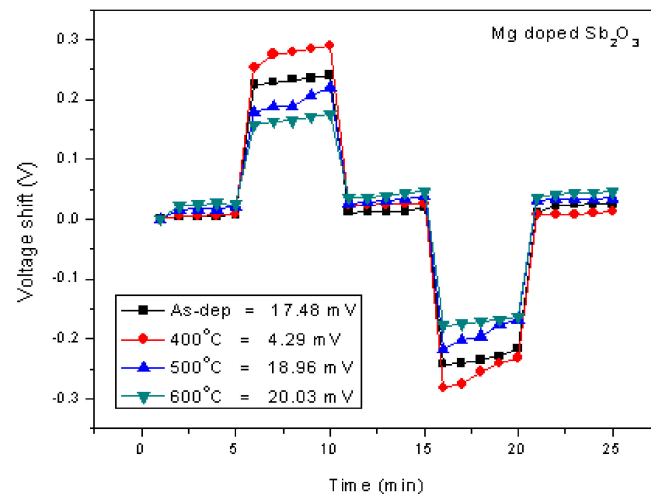
(**b**)

Figure 8. *Cont.*

(**c**)

(**d**)

Figure 8. The hysteresis of (**a**) the Ti-doped Sb_2O_3 EIS membranes and (**b**) the Mg-doped Sb_2O_3 EIS membranes annealed in different conditions during a pH loop of 7→4→7→10. The drift voltage measurements of (**c**) the Ti-doped Sb_2O_3 EIS membranes and (**d**) the Mg-doped Sb_2O_3 EIS membranes annealed in different conditions.

To study stability and long-term reliability issues, the hysteresis voltages and the drift voltages were assessed. To calculate the hysteresis voltages, the samples were immersed in solutions with various pH values of 7, 4, 7, 10 in an alternating cycle with an immersion time of 5 min. The hysteresis voltage of the Ti-doped and Mg-doped samples with various annealing treatments are shown in Figure 8a,b, respectively. Consistent with the material characterizations and sensing measurements, the hysteresis voltages for the Ti-doped sample and the Mg-doped sample annealed at 400 °C had the lowest values of 27.28, 4.84 and 4.29 mV, respectively. Mg doping incorporated with annealing at 400 °C had the most reliable response. Since the dangling bonds and traps might capture H^+ or OH^- ions in solutions, a membrane of better material quality might exhibit lower hysteresis voltages. Furthermore, to evaluate the capacitor's long-term reliability, all of the tested samples were immersed in pH7 buffer solutions for 12 h, and the drift voltages were calculated. Similarly, the hysteresis voltages for the Ti-doped sample and the Mg-doped sample annealed at 400 °C had the smallest values of 3.01 and 1.99 mV/hr, respectively,

as shown in Figure 8c,d. Since post-annealing at 400 °C incorporating Mg doping could effectively reduce vacancies and defects, the drift voltage of the Mg-doped sample annealed at 400 °C was greatly suppressed. These reliability tests were consistent with all of the other electrical measurements and material analyses [62].

Finally, to compare the sensing sensitivity of different ions on the EIS structure, the sensitivity and linearity of the K^+ and Na+ ions of the undoped, the Ti-doped and Mg-doped samples were measured. As shown in Figure 9a–f, the sensitivity and linearity measurement of K^+ ion for the samples reveal that the Mg-doped sample annealed at 400 °C had the optimized sensitivity of 17.3 mV/pK and linearity of 96.15%.
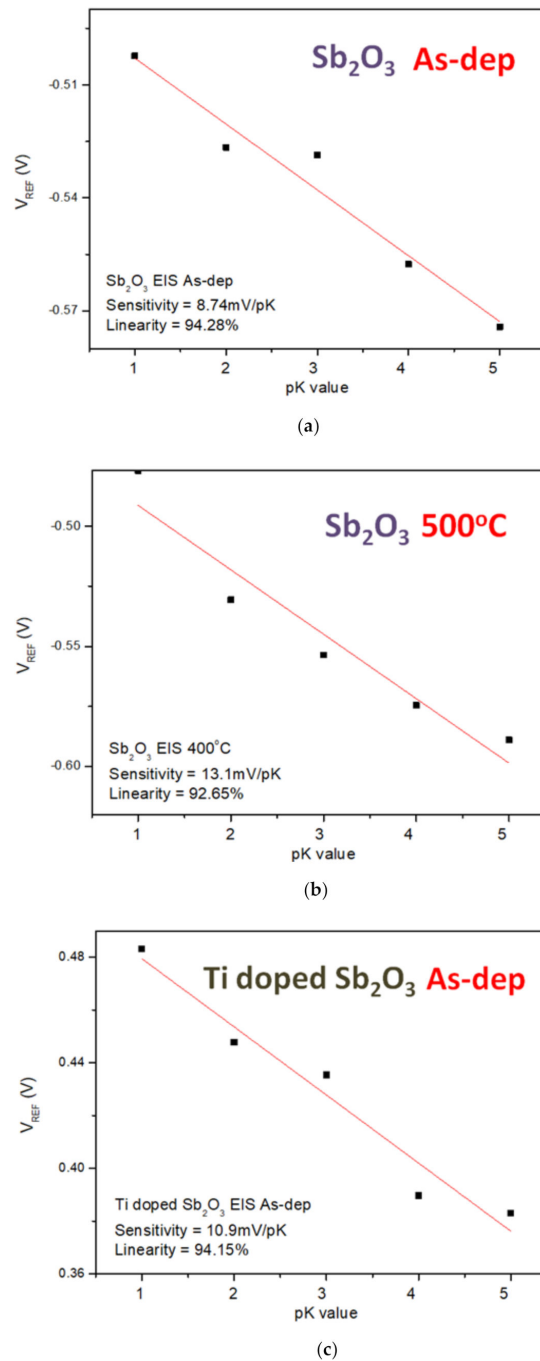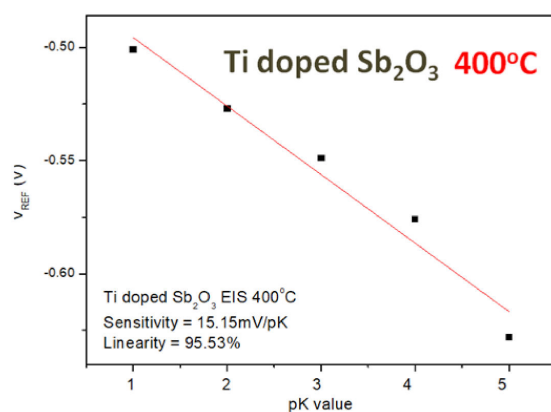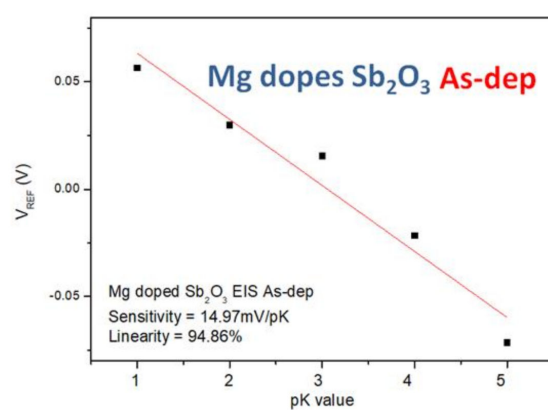

(a)

(b)

(c)

Figure 9. *Cont.*

(d)

(e)
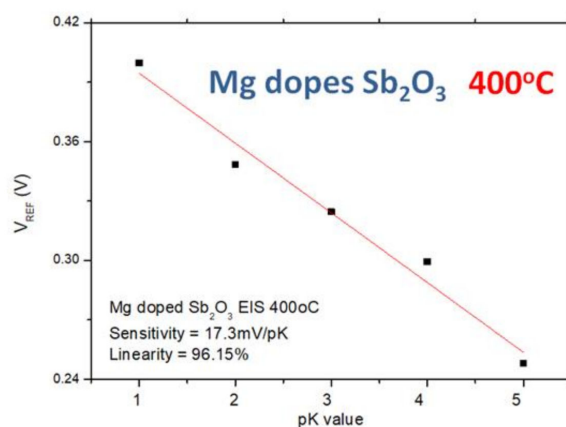
(f)

Figure 9. The K$^+$ sensing behaviors of (**a**) the as-deposited Sb$_2$O$_3$ sensing membrane, (**b**) the Sb$_2$O$_3$ sensing membrane annealed at 500 °C, (**c**) the as-deposited Ti-doped Sb$_2$O$_3$ sensing membrane, (**d**) the Ti-doped Sb$_2$O$_3$ sensing membrane annealed at 400 °C, (**e**) the as-deposited Mg-doped sensing membrane and (**f**) the Mg-doped O$_3$ sensing membrane annealed at 400 °C.

Similarly, the sensitivity and linearity measurements of the Na$^+$ ion for the samples reveal that the Mg-doped sample annealed at 400 °C had an optimized sensitivity of 21.01 mV/pK and a linearity of 96.15%, as shown in Figure 10a–f. Since the radius and mass of H$^+$ ions are much smaller than the radius and mass of K$^+$ and Na$^+$, the sensitivity of the K$^+$ and Na$^+$ ions is smaller than that of the H$^+$ ions.

Finally, the sensitivity, linearity, hysteresis characteristics and drift characteristics of the appropriately annealed undoped, Ti-doped and Mg-doped Sb$_2$O$_3$ membranes were com-

pared. The Mg-doped Sb_2O_3 membranes annealed at 400 °C still had the most preferable sensing characteristics compared with all of the other samples, as shown in Figure 11.

(a)

(b)

(c)
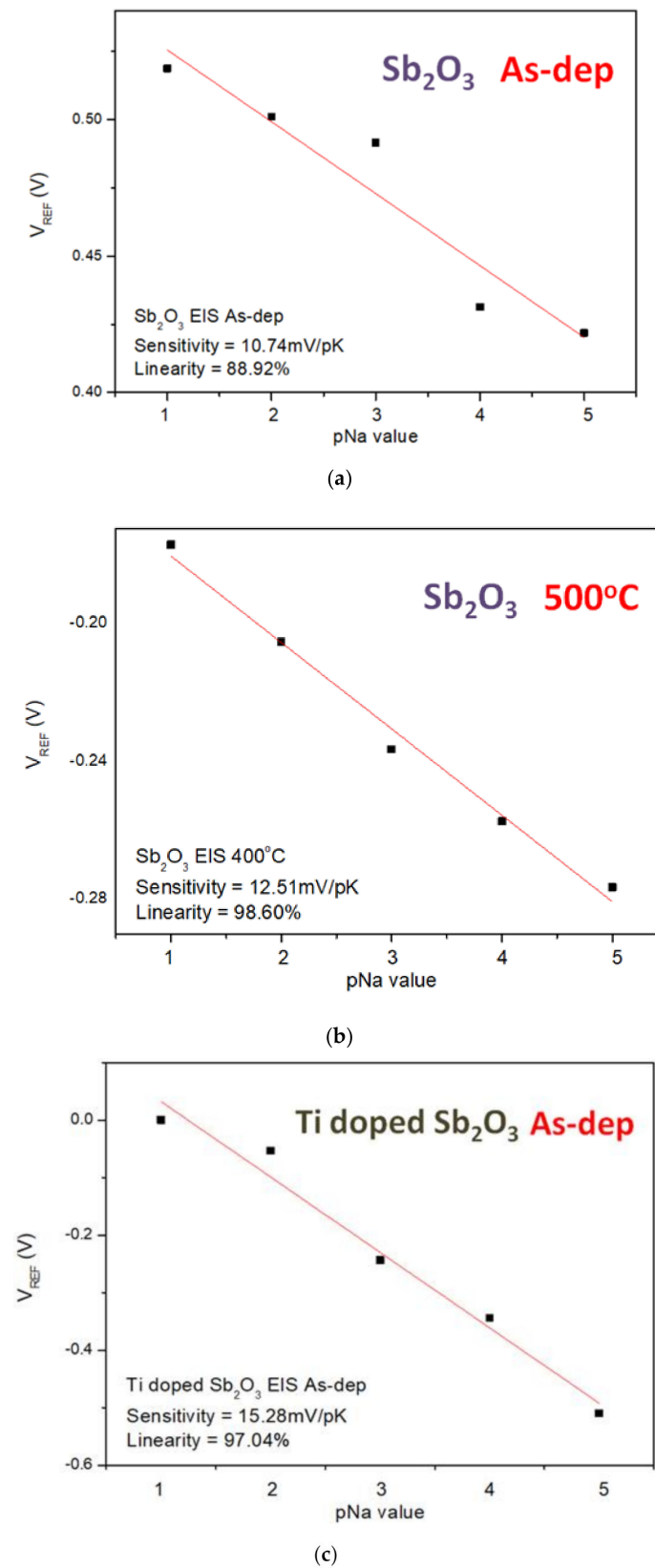
Figure 10. *Cont.*
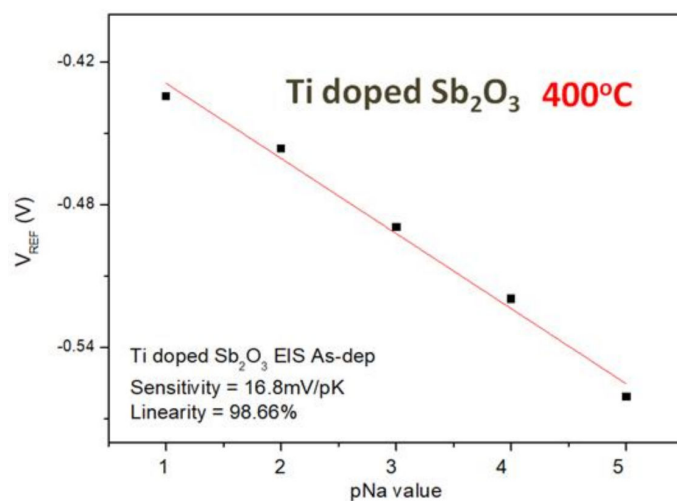
(**d**)
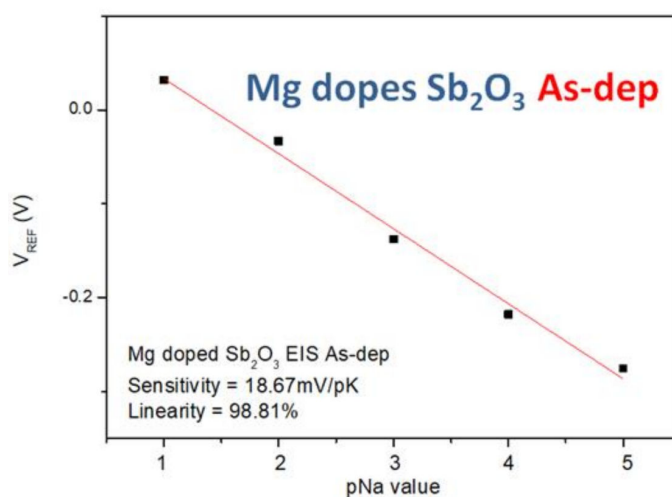
(**e**)
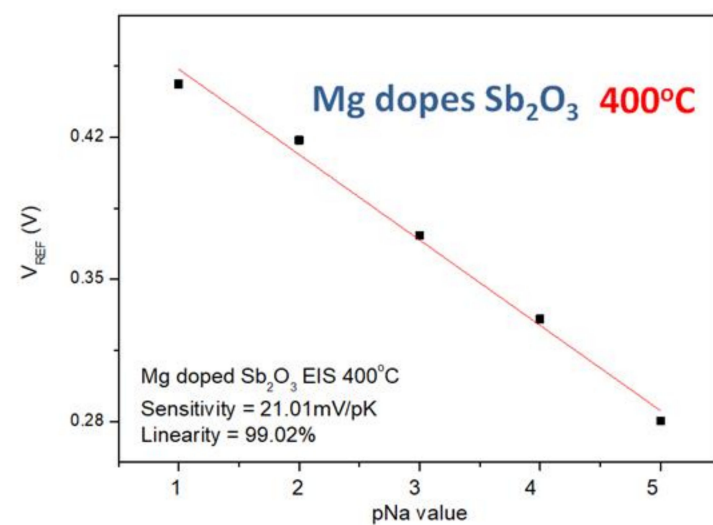
(**f**)

Figure 10. The Na$^+$ sensing behaviors of (**a**) the as-deposited Sb$_2$O$_3$ sensing membrane, (**b**) the Sb$_2$O$_3$ sensing membrane annealed at 500 °C, (**c**) the as-deposited Ti-doped Sb$_2$O$_3$ sensing membrane, (**d**) the Ti-doped Sb$_2$O$_3$ sensing membrane annealed at 400 °C, (**e**) the as-deposited Mg-doped sensing membrane and (**f**) the Mg-doped O$_3$ sensing membrane annealed at 400 °C.

EIS	Sb_2O_3 (O₂) (500°C)	Ti-doped Sb_2O_3 (O₂) (400°C)	Mg-doped Sb_2O_3 (O₂) (400°C)
pH sensitivity (mV/pH)	51.96	54.08	60.17
Linearty (%)	98.10	99.44	99.06
Hysteresis voltage (mV)	13.82	4.84	4.29
Drift rate (mV/hr)	7.25	3.01	1.99

Figure 11. Comparison of the sensing behaviors of the appropriately annealed, undoped, Ti-doped and Mg-doped Sb_2O_3 membranes.

4. Conclusions

In this study, undoped, Ti-doped and Mg-doped Sb_2O_3 sensing membranes with various annealing conditions were fabricated. Multiple material characterizations and sensing measurements were conducted to study the annealing and doping effects on the membranes. The results indicate that Mg doping incorporating annealing at an appropriate temperature of 400 °C could optimize the material quality and enhance the sensing behaviors due to the suppression of silicate, the enhancement of crystallization, the boosting of sensing factors and the removal of defects. Mg-doped Sb_2O_3-based membranes with appropriate annealing are promising for future industrial ion-sensing devices and for possible integration with Sb_2O_3-based devices.

Author Contributions: Conceptualization, C.-H.K., Y.-W.K., M.-L.L., L.J.-H.L. and H.C.; methodology, C.-H.K. and H.C.; data curation, K.-L.C.; writing—original draft preparation, J.-R.C., S.-M.C. and H.C.; writing—review and editing, H.C.; visualization, H.C.; supervision, C.-H.K. and H.C.; project administration, H.C.; funding acquisition, M.-L.L. and H.C. All authors have read and agreed to the published version of the manuscript.

Institutional Review Board Statement: Not applicable.

Informed Consent Statement: Not applicable.

Data Availability Statement: The data used to support the findings of this study are available from the corresponding author upon request.

Conflicts of Interest: There are no conflicts of interest to declare. The funders had no role in the design of the study; in the collection, analyses or interpretation of data; in the writing of the manuscript; or in the decision to publish the results.

References

1. Pan, T.-M.; Lin, J.-C.; Wu, M.-H.; Lai, C.-S. Structural properties and sensing performance of high-k Nd_2TiO_5 thin layer-based electrolyte–insulator–semiconductor for pH detection and urea biosensing. *Biosens. Bioelectron.* **2009**, *24*, 2864–2870. [CrossRef]
2. Schöning, M.J. Playing around with field-effect sensors on the basis of EIS structures, LAPS and ISFETs. *Sensors* **2005**, *5*, 126–138. [CrossRef]

3. Kao, C.-H.; Chen, H.; Kuo, L.-T.; Wang, J.-C.; Chen, Y.-T.; Chu, Y.-C.; Chen, C.-Y.; Lai, C.-S.; Chang, S.W.; Chang, C.W. Multi-analyte biosensors on a CF_4 plasma treated Nb_2O_5-based membrane with an extended gate field effect transistor structure. *Sens. Actuators B Chem.* **2013**, *194*, 419–426. [CrossRef]

4. Kao, C.H.; Chen, H.; Lee, M.L.; Liu, C.C.; Ueng, H.-Y.; Chu, Y.C.; Chen, C.B.; Chang, K.M. Effects of N_2 and O_2 annealing on the multianalyte biosensing characteristics of CeO_2-based electrolyte–insulator–semiconductor structures. *Sens. Actuators B Chem.* **2014**, *194*, 503–510. [CrossRef]

5. Tudorache, F.; Tigau, N.; Condurache-Bota, S. Humidity sensing characteristics of Sb_2O_3 thin films with transitional electrical behavior. *Sens. Actuators A Phys.* **2018**, *285*, 134–141. [CrossRef]

6. Kwo, J.; Hong, M.; Kortan, A.R. Properties of high κ gate dielectrics Gd_2O_3 and Y_2O_3 for Si. *J. Appl. Phys.* **2001**, *89*, 3920–3927. [CrossRef]

7. Ott, J.; Lorenz, A.; Harrer, M. The influence of Bi_2O_3 and Sb_2O_3 on the electrical properties of ZnO-based varistors. *J. Electroceram.* **2001**, *6*, 135–146. [CrossRef]

8. Mestl, G.; Ruiz, P.; Delmon, B.; Knozinger, H. Sb_2O_3/Sb_2O_4 in reducing/oxidizing environments: An in situ Raman spectroscopy study. *J. Phys. Chem.* **1994**, *98*, 11276–11282. [CrossRef]

9. Le, T.; Hai, L.C.; Hung, T.T.; Phuong, B. Multiwall carbon nanotube modified by antimony oxide (Sb_2O_3/MWCNTs) paste electrode for the simultaneous electrochemical detection of cadmium and lead ions. *Microchem. J.* **2020**, *153*, 104456.

10. Gonçalves, R.A.; Baldan, M.R.; Ciapina, E.G.; Berengue, O.M. Nanostructured Pd/Sb_2O_3: A new and promising fuel cell electrocatalyst and non-enzymatic amperometric sensor for ethanol. *Appl. Surf. Sci.* **2019**, *491*, 9–15. [CrossRef]

11. Wang, Q.; Wu, H.; Wang, Y. Ex-situ XPS analysis of yolk-shell Sb_2O_3/WO_3 for ultra-fast acetone resistive sensor. *J. Hazard. Mater.* **2021**, *412*, 125175. [CrossRef]

12. Stojanović, Z.S.; Đurović, A.D.; Ashrafi, A.M.; Koudelková, Z.; Zítka, O.; Richtera, L. Highly sensitive simultaneous electrochemical determination of reduced and oxidized glutathione in urine samples using antimony trioxide modified carbon paste electrode. *Sens. Actuators B Chem.* **2020**, *318*, 128141. [CrossRef]

13. Bai, H.; Guo, H.; Wang, J. Hydrogen gas sensor based on SnO_2 nanospheres modified with Sb_2O_3 prepared by one-step solvothermal route. *Sens. Actuators B Chem.* **2021**, *331*, 129441. [CrossRef]

14. Majidian, M.; Raoof, J.B.; Hosseini, S.R.; Fischer, J.; Barek, J. Determination of 8-hydroxy-7-iodo-5-quinoline sulfonic acid (HIQSA) at renewable electrode with Sb_2O_3/MWCNT-TiO_2 nanohybrid. *J. Electroanal. Chem.* **2020**, *858*, 113775. [CrossRef]

15. Li, Z.; Zong, L.; Liu, H.; Yao, Z.; Sun, Y.; Li, Z. A solid-state Sb/Sb_2O_3 biosensor for the in situ measurement of extracellular acidification associated with the multidrug resistance phenotype in breast cancer cells. *Anal. Methods* **2018**, *10*, 4445–4453. [CrossRef]

16. Rahman, M.M.; Alam, M.M.; Asiri, A.M. Development of an efficient phenolic sensor based on facile Ag_2O/Sb_2O_3 nanoparticles for environmental safety. *Nanoscale Adv.* **2018**, *1*, 696–705. [CrossRef]

17. Kotchasak, N.; Inyawilert, K.; Wisitsorrat, A. Chemophysical acetylene-sensing mechanisms of $Sb_2O_3/NaWO_4$-doped WO_3 heterointerfaces. *Phys. Chem. Chem. Phys.* **2020**, *22*, 20482–20498. [CrossRef]

18. Sukul, P.P.; Kumar, K. Afruitful demonstration in sensors based on upconversion luminescence of Yb^{3+}/Er^{3+} codoped Sb_2O_3-WO_3-Li_2O (SWL) glass-ceramic. *Mater. Res. Express* **2016**, *3*, 076207. [CrossRef]

19. Sen, S.; Nilabh, A.; Kundu, S. Room temperature acetone sensing performance of Pt/Sb_2O_3 impregnated Fe2O3 thin film: Noninvasive diabetes detection. *Microchem. J.* **2021**, *165*, 106111. [CrossRef]

20. Tigau, N.; Ciupina, V.; Prodan, G. The effect of substrate temperature on the optical properties of polycrystalline Sb_2O_3 thin films. *J. Cryst. Growth* **2005**, *277*, 529–535. [CrossRef]

21. Wang, L.; Gao, C.; Dai, L. Improvement of Al^{3+} ion conductivity by F doping of $(Al_{0.2}Zr_{0.8})_{4/3.8}$ NbP_3O_{12} solid electrolyte for mixed potential NH3 sensors. *Ceram. Int.* **2018**, *44*, 8983–8991. [CrossRef]

22. Palmer, M.; Masikini, M.; Jiang, L.W. Enhanced electrochemical glucose sensing performance of CuO: NiO mixed oxides thin film by plasma assisted nitrogen doping. *J. Alloy. Compd.* **2021**, *853*, 156900. [CrossRef]

23. Lu, J.; Lu, Y.-M.; Tasi, S.; Hsiung, T.-L.; Wang, H.P.; Jang, L. Conductivity enhancement and semiconductor–metal transition in Ti-doped ZnO films. *Opt. Mater.* **2007**, *29*, 1548–1552. [CrossRef]

24. Lin, C.F.; Kao, C.H.; Lin, C.Y.; Liu, Y.W.; Wang, C.H. The electrical and physical characteristics of Mg-doped ZnO sensing membrane in EIS (electrolyte–insulator–semiconductor) for glucose sensing applications. *Results Phys.* **2020**, *16*, 102976. [CrossRef]

25. Liston, E.M. Plasma Treatment for Improved Bonding: A Review. *J. Adhes.* **1989**, *30*, 199–218. [CrossRef]

26. Tanaka, T.; Nagatomo, T.; Kawasaki, D.; Nishio, M.; Guo, Q.; Wakahara, A.; Yoshida, A.; Ogawa, H. Preparation of Cu_2ZnSnS_4 thin films by hybrid sputtering. *J. Phys. Chem. Solids* **2005**, *66*, 1978–1981. [CrossRef]

27. Van Dover, R. Amorphous lanthanide-doped TiO_x dielectric films. *Appl. Phys. Lett.* **1999**, *74*, 3041–3043. [CrossRef]

28. Wang, Y.; Nan, C.-W. Enhanced ferroelectricity in Ti-doped multiferroic $BiFeO_3$ thin films. *Appl. Phys. Lett.* **2006**, *89*, 52903. [CrossRef]

29. Pan, T.-M.; Lin, J.-C. A TiO_2/Er_2O_3 stacked electrolyte/insulator/semiconductor film pH-sensor for the detection of urea. *Sens. Actuators B Chem.* **2009**, *138*, 474–479. [CrossRef]

30. Chou, J.C.; Liao, L.P. Study of TiO_2 thin films for ion sensitive field effect transistor application with rf sputtering deposition. *Jpn. J. Appl. Phys.* **2004**, *43*, 61. [CrossRef]

31. Isabel, A.P.S.; Kao, C.H.; Mahanty, R.K.; Wu, Y.C.S.; Li, C.Y.; Lin, C.Y.; Lin, C.F. Sensing and structural properties of Ti-doped tin oxide (SnO_2) membrane for bio-sensor applications. *Ceram. Int.* **2017**, *43*, 10386–10391. [CrossRef]

32. Lee, M.L.; Wang, J.C.; Kao, C.H.; Chen, H.; Lin, C.Y.; Chang, C.W.; Mahanty, R.K.; Lin, C.F.; Chang, K.M. Comparison of ZnO and Ti-doped ZnO sensing membrane applied in electrolyte-insulator-semiconductor structure. *Ceram. Int.* **2018**, *44*, 6081–6088. [CrossRef]

33. Kao, C.-H.; Su, Y.-L.; Liao, W.-J.; Li, M.-H.; Chan, W.-L.; Tsai, S.-C.; Chen, H. Effects of CF_4 Plasma Treatment on Indium Gallium Oxide and Ti-doped Indium Gallium Oxide Sensing Membranes in Electrolyte–Insulator–Semiconductors. *Crystals* **2020**, *10*, 810. [CrossRef]

34. Kao, C.-H.; Liu, C.S.; Xu, C.Y.; Lin, C.F.; Chen, H. Ti-doped indium gallium oxide electrolyte–insulator–semiconductor membranes for multiple ions and solutes detectors. *J. Mater. Sci. Mater. Electron.* **2019**, *30*, 20596–20604. [CrossRef]

35. Kao, C.H.; Chang, C.W.; Chen, Y.T.; Su, W.M.; Lu, C.C. Influence of NH_3 plasma and Ti doping on pH-sensitive CeO_2 electrolyte-insulator-semiconductor biosensors. *Sci. Rep.* **2017**, *7*, 2405.

36. Nakarmi, M.; Kim, K.; Khizar, M.; Fan, Z.; Lin, J.; Jiang, H. Electrical and optical properties of Mg-doped $Al_{0.7}Ga_{0.3}$ N alloys. *Appl. Phys. Lett.* **2005**, *86*, 092108. [CrossRef]

37. Kılınç, N.; Arda, L.; Öztürk, S.; Öztürk, Z. Structure and electrical properties of Mg-doped ZnO nanoparticles. *Cryst. Res. Technol.* **2010**, *45*, 529–538. [CrossRef]

38. Hautakangas, S.; Oila, J.; Alatalo, M.; Saarinen, K.; Liszkay, L.; Seghier, D.; Gislason, H.P. Vacancy Defects as Compensating Centers in Mg-Doped GaN. *Phys. Rev. Lett.* **2003**, *90*, 137402. [CrossRef] [PubMed]

39. Mohar, R.S.; Sugihartono, I.; Fauzia, V.; Umar, A.A. Dependence of optical properties of Mg-doped ZnO nanorods on Al dopant. *Surf. Interfaces* **2020**, *19*, 100518. [CrossRef]

40. Kao, C.H.; Liu, C.S.; Lu, S.H.; Tsai, S.C.; Chan, W.L.; Lin, B.H.; Lin, C.F.; Chen, H.; Han, J. Multianalyte Mg-Doped InGaZnO Electrolyte-Insulator-Semiconductor Biosensors and Multiple Material Characterizations of Membrane Nanostructures. *IEEE Sens. J.* **2020**, *20*, 10653–10663. [CrossRef]

41. Lin, C.F.; Kao, C.H.; Lin, C.Y.; Chen, K.L.; Lin, Y.H. NH_3 Plasma-Treated Magnesium Doped Zinc Oxide in Biomedical Sensors with Electrolyte–Insulator–Semiconductor (EIS) Structure for Urea and Glucose Applications. *Nanomaterials* **2020**, *10*, 583. [CrossRef]

42. Al-Khalqi, E.M.; Hamid, M.A.A.; Al-Hardan, N.H.; Keng, L.K. Highly Sensitive Magnesium-Doped ZnO Nanorod pH Sensors Based on Electrolyte–Insulator–Semiconductor (EIS) Sensors. *Sensors* **2021**, *21*, 2110. [CrossRef]

43. Knopfmacher, O.; Tarasov, A.; Fu, W.; Wipf, M.; Niesen, B.; Calame, M.; Schönenberger, C. Nernst Limit in Dual-Gated Si-Nanowire FET Sensors. *Nano Lett.* **2010**, *10*, 2268–2274. [CrossRef]

44. Harame, D.L.; Bousse, L.J.; Shott, J.D.; Meindl, D.J. Ion-sensing devices with silicon nitride and borosilicate glass insulators. *IEEE Trans. Electron. Devices* **1987**, *34*, 1700–1707. [CrossRef]

45. Chang, L.-B.; Ko, H.-H.; Lee, Y.-L.; Lai, C.-S.; Wang, C.-Y. The Electrical and pH-Sensitive Characteristics of Thermal Gd_2O_3/SiO_2-Stacked Oxide Capacitors. *J. Electrochem. Soc.* **2006**, *153*, G330. [CrossRef]

46. Khan, M.I.; Mukherjee, K.; Shoukat, R.; Dong, H. A review on pH sensitive materials for sensors and detection methods. *Microsyst. Technol.* **2017**, *23*, 4391–4404. [CrossRef]

47. Manjakkal, L.; Szwagierczak, D.; Dahiya, R. Metal oxides based electrochemical pH sensors: Current progress and future perspectives. *Prog. Mater. Sci.* **2020**, *109*, 100635. [CrossRef]

48. Kumar, N.; Kumar, J.; Panda, S. Back-Channel Electrolyte-Gated a-IGZO Dual-Gate Thin-Film Transistor for Enhancement of pH Sensitivity Over Nernst Limit. *IEEE Electron. Device Lett.* **2016**, *37*, 500–503. [CrossRef]

49. Poghossian, A. The super-Nernstian pH sensitivity of Ta_2O_5-gate ISFETs. *Sens. Actuators B Chem.* **1992**, *7*, 367–370. [CrossRef]

50. Bousse, L.; de Rooij, N.F.; Bergveld, P. Operation of chemically sensitive field-effect sensors as a function of the insulator-electrolyte interface. *IEEE Trans. Electron. Devices* **1983**, *30*, 1263–1270. [CrossRef]

51. Fung, C.D.; Cheung, P.W.; Ko, W.H. A generalized theory of an electrolyte-insulator-semiconductor field-effect transistor. *IEEE Trans. Electron. Devices* **1986**, *33*, 8–18. [CrossRef]

52. Van Hal, R.; Eijkel, J.; Bergveld, P. A novel description of ISFET sensitivity with the buffer capacity and double-layer capacitance as key parameters. *Sens. Actuators B Chem.* **1995**, *24*, 201–205. [CrossRef]

53. Oldham, K.B. A Gouy–Chapman–Stern model of the double layer at a (metal)/(ionic liquid) interface. *J. Electroanal. Chem.* **2008**, *613*, 131–138. [CrossRef]

54. Pruneanu, S.; Boughriet, A.; Henderson, A.; Malins, C.; Ali, Z.; Olenic, L. Impedimetric measurements for monitoring avidin-biotin interaction on self-assembled monolayer. *Part. Sci. Technol.* **2008**, *26*, 136–144. [CrossRef]

55. Zeng, R.-H.; Li, W.-S.; Dong-Sheng, L.; Huang, Q.-M.; Zhao, L.-Z. Insertion/removal kinetics of lithium ion in spinel $LiCu_xMn_{2-x}O_4$. *Trans. Nonferrous Met. Soc. China* **2007**, *17*, 1312–1318. [CrossRef]

56. Divya, K.; Abraham, K. Ag nanoparticle decorated Sb_2O_3 thin film: Synthesis, characterizations and application. *Nano Express* **2020**, *1*, 020005. [CrossRef]

57. Chen, X.; Wang, L.; Ma, F.; Wang, T.; Han, J.; Huang, Y.; Li, Q. Core@shell $Sb@Sb_2O_3$ nanoparticles anchored on 3D nitrogen-doped carbon nanosheets as advanced anode materials for Li-ion batteries. *Nanoscale Adv.* **2020**, *2*, 5578–5583. [CrossRef]

58. Yule, Z.; Shouan, Z.; Tao, L. Drift characteristics of pH-ISFET output. *Chin. J. Semiconduct.* **1994**, *12*, 838–843.

59. Tigau, N.; Ciupina, V.; Prodan, G. Structural, optical and electrical properties of Sb_2O_3 thin films with different thickness. *J. Optoelectron. Adv. Mater.* **2006**, *8*, 37.
60. Chou, J.-C.; Weng, C.-Y. Sensitivity and hysteresis effect in Al_2O_3 gate pH-ISFET. *Mater. Chem. Phys.* **2001**, *71*, 120–124. [CrossRef]
61. Bousse, L.; van den Vlekkert, H.; de Rooij, N. Hysteresis in al_2o_3-gate isfets. *Sens. Actuators B Chem.* **1990**, *2*, 103–110. [CrossRef]
62. Mayergoyz, I. Mathematical models of hysteresis. *IEEE Trans. Magn.* **1986**, *22*, 603–608. [CrossRef]